

A NUMERICAL STUDY OF THE BREAKOUT MODEL FOR CORONAL MASS EJECTION INITIATION

P. MACNEICE,¹ S. K. ANTIOCHOS,² A. PHILLIPS,¹ D. S. SPICER,³ C. R. DEVORE,² AND K. OLSON⁴

Received 2003 December 4; accepted 2004 July 1

ABSTRACT

A leading theory for the initiation of coronal mass ejections (CMEs) is the breakout model, in which magnetic reconnection above a filament channel is responsible for disrupting the coronal magnetic field. We present the first simulations of the complete breakout process including the initiation, the plasmoid formation and ejection, and the eventual relaxation of the coronal field to a more potential state. These simulations were performed using a new numerical code that solves the numerical cavitation problems that prevented previous simulations from calculating a complete ejection. Furthermore, the position of the outer boundary in the new simulations is increased out to $30 R_{\odot}$, which enables determination of the full structure and dynamics of the ejected plasmoid. Our results show that the ejection occurs at a speed on the order of the coronal Alfvén speed and hence that the breakout model can produce fast CMEs. Another key result is that the ejection speed is not sensitive to the refinement level of the grid used in the calculations, which implies that, at least for the numerical resistivity of these simulations, the speed is not sensitive to the Lundquist number. We also calculate, in detail, the helicity of the system and show that the helicity is well conserved during the breakout process. Most of the helicity is ejected from the Sun with the escaping plasmoid, but a significant fraction (of order 10%) remains in the corona. The implications of these results for observation and prediction of CMEs and eruptive flares is discussed.

Subject headings: Sun: corona — Sun: coronal mass ejections (CMEs) — Sun: flares

1. INTRODUCTION

The most energetic and most dramatic manifestations of solar activity are the giant disruptions of magnetic field and plasma known as coronal mass ejections (CMEs)/eruptive flares. A large CME can consist of more than 10^{16} g of coronal plasma accelerated to more than 1000 km s^{-1} on a timescale of ~ 1000 s. (In this paper, we emphasize fast CMEs typical of a major CME/eruptive flare event, since these are the most important for space weather and the most difficult to explain theoretically.) The overriding problem in understanding the physics of fast CMEs is accounting for their explosive nature, a topic of intense theoretical study (e.g., Sturrock 1989; van Ballegoijen & Martens 1989; Forbes & Isenberg 1991; Moore & Roumeliotis 1992; Low & Smith 1993; Mikić & Linker 1994; Wu et al. 1995; Wolfson & Saran 1998; Amari et al. 2000; Priest & Forbes 2000; Chen 2001). The basic energy source must be magnetic stress that comes through the photosphere, either by direct motions or by emergence of prestressed flux. However, the coronal system is driven very slowly: $\sim 1 \text{ km s}^{-1}$ footpoint speeds compared to its characteristic Alfvén speed of $\sim 1000 \text{ km s}^{-1}$. Furthermore, the coronal field is free to expand outward quasi-statically, which is the evolution usually observed and is expected from analytic theory of the ideal behavior of a force-free coronal magnetic field (Aly 1984, 1991; Sturrock 1991).

Because of these observational constraints, most of the present models postulate that CMEs represent the explosive

release of magnetic energy stored in the corona, specifically, in the strongly nonpotential magnetic field of a sheared neutral line, or filament channel (see recent reviews by Low 1996; Forbes 2000; Klimchuk 2001; Lin et al. 2003). Although a filament eruption may not be observed with every CME, it is well known that all major solar activity such as flares and CMEs are associated with a sheared neutral line (e.g., Patten & Hagyard 1986; Schmieder et al. 1996). Furthermore, filament channels are the only locations in the Sun's corona where the field appears to be strongly nonpotential and hence where large amounts of free energy can be stored. It appears highly likely, therefore, that the underlying cause of CMEs, eruptive flares, and filament ejections is the disruption of a force balance between the upward pressure of the sheared filament channel field and the downward tension of overlying coronal field that is quasi-potential.

A key point is that the upward pressure cannot increase rapidly, because the magnetic shear/twist is produced by the slow photospheric evolution (shear flows and/or flux emergence). Therefore, explosive events such as CMEs must be due fundamentally to the catastrophic removal of the downward magnetic tension of the overlying coronal field. Recent theory and simulation has focused on magnetic reconnection as the mechanism for the removal of the magnetic tension (Low 1996; Forbes 2000; Klimchuk 2001; Lin et al. 2003). Only two reconnection models have been proposed that have successfully demonstrated explosive eruption with full MHD numerical simulations: flux cancellation (Amari et al. 2000) and magnetic breakout (Antiochos et al. 1999). In the cancellation model, reconnection is postulated to occur at the photospheric neutral line below a filament channel, producing a twisted flux rope in the corona and eventually leading to a loss of equilibrium (Forbes 2000). In the breakout model, reconnection at a null point above a filament channel leads to the removal of overlying flux and to an explosive outward expansion (Antiochos 1998, 1999). At present, neither model

¹ Physics Department, Drexel University, Philadelphia, PA 19104; macneice@alfven.gsfc.nasa.gov, phillips@sommerfeld.gsfc.nasa.gov.

² Naval Research Laboratory, Washington, DC 20375; antiochos@nrl.navy.mil, devore@lcp.nrl.navy.mil.

³ NASA Goddard Space Flight Center, Greenbelt, MD 20771; spicer@gauss.gsfc.nasa.gov.

⁴ University of Maryland, Baltimore County, Baltimore, MD 21250; olson@bohr.gsfc.nasa.gov.

can be considered to have been either definitively verified or refuted by the observations. However, there have been a number of studies recently that strongly support a breakout interpretation for some well-observed CME/eruptive flare events (e.g., Aulanier et al. 2000; Sterling & Moore 2001).

It should be emphasized that both models predict a similar evolution once the eruption is well underway. The rapid upward expansion of the filament channel field causes a current sheet to form below the erupting field, resulting in strong reconnection there. This reconnection produces a highly twisted plasmoid that escapes from the corona and leaves behind the hot X-ray, flare loops, as in the standard model (Carmichael 1964; Sturrock 1966; Hirayama 1974; Kopp & Pneuman 1976). An important issue for any model is the speed of the escaping plasmoid. In order to account for fast CMEs, the erupting plasma must be ejected from the Sun at speeds of order the Alfvén velocity. But the previous numerical studies of breakout could not calculate the actual ejection itself (Antiochos et al. 1999). These studies were a critically important first step, because they showed how a multipolar magnetic topology could contain sufficient free energy to open up the filament channel field and still be compatible with the Aly-Sturrock energy limit (Aly 1991; Sturrock 1991), but they could not verify that a fast CME would result. The problem was that once the eruption picked up significant speed, the reconnection at the rapidly moving coronal null led to numerical cavitation there (i.e., very low densities), and the simulations developed severe numerical inaccuracies.

Our goal in this paper is to calculate the complete evolution of the breakout eruption, including the formation and escape of the plasmoid. The main issues that we focus on are the speed of the eruption and the evolution of the magnetic helicity in the corona. We use the exact same 2.5-dimensional geometry and magnetic topology as in Antiochos et al. (1999), but we employ a more robust numerical code that mitigates the effects of cavitation by applying a mass diffusion at grid cells where the density exhibits too large a density drop. In addition, we extend the computational domain out to $30 R_{\odot}$ so as to be able to follow the evolution of the plasmoid well after it has been ejected from the corona. A larger outer radius also helps minimize any effects from the boundary conditions there. The physical model and the code are described in detail below.

2. DESCRIPTION OF NUMERICAL MODEL

Our model follows that described in Antiochos et al. (1999) in most details, and so we limit our description of it to a summary of the essential features and a detailed exposition of all significant modifications.

The idealized model has a complex initial field geometry with azimuthal symmetry. It has four flux systems, as shown in the first panel of Figure 1. An inner flux system is centered on the equator. Mid-latitude flux systems are centered on latitude $\pm 45^\circ$, and at large radius there is an overlying dipole system. These four flux systems are bounded by two separatrix surfaces that intersect in the corona at an X-point (actually an X-line due to the axisymmetry). A footpoint shear is applied to the inner equatorial flux system, which causes it to expand outward and push against the overlying field, deforming the X-point to a current sheet. Reconnection between the equatorial and overlying systems causes flux in the inner region to be transferred to the mid-latitude flux systems, which induces the remaining inner flux system to expand outward even faster. This feedback causes an ever-increasing outward expansion of the field that

eventually leads to an explosive opening of the overlying field, formation of a lower X-line and flux rope, and escape of some of the sheared inner flux to infinity.

2.1. Equations

To model this scenario, we solve the equations of ideal MHD including gravitational acceleration:

$$\frac{\partial \rho}{\partial t} + \nabla \cdot (\rho \mathbf{v}) = 0, \quad (1)$$

$$\frac{\partial}{\partial t}(\rho \mathbf{v}) + \nabla \cdot (\rho \mathbf{v} \mathbf{v}) + \nabla p = \frac{1}{4\pi}(\nabla \times \mathbf{B}) \times \mathbf{B} - \rho \mathbf{g}, \quad (2)$$

$$\frac{\partial U}{\partial t} + \nabla \cdot (U \mathbf{v}) + p \nabla \cdot \mathbf{v} = 0, \quad (3)$$

and

$$\frac{\partial \mathbf{B}}{\partial t} = \nabla \times (\mathbf{v} \times \mathbf{B}), \quad (4)$$

where ρ is mass density, \mathbf{v} is velocity, p is gas pressure, $U = 3p/2$ is the internal energy, \mathbf{B} is magnetic induction, and $\mathbf{g} = g_0 \mathbf{e}_r / r^2$ is gravitational acceleration.

2.2. Numerical Techniques

Our numerical code is a modified version of the code described by DeVore (1991). It uses a multidimensional flux-corrected transport (FCT) algorithm in spherical coordinates and guarantees preserving the divergence-free condition on the magnetic field to machine accuracy. The code is second-order accurate in space and time for a uniformly spaced grid.

We have modified the application of the flux limiter to achieve greater consistency in its use across the set of equations. The FCT algorithm can be viewed as a combination of high- and low-order algorithms. The low-order algorithm is the same as the high-order algorithm but has a known explicit diffusion added to ensure that the low-order solution retains positivity and monotonicity. For a given time step, the solution for each equation is computed using the low-order scheme. Antidiffusive fluxes are then computed that remove as much of this additional diffusion as possible, under the constraint that the antidiffusion step cannot introduce new extrema into the solution or accentuate any existing extrema. For each equation, the fraction of the antidiffusive flux that can be applied without violating this constraint is recorded. We then take the minimum of the fractions associated with the mass and energy densities and apply these to limit the antidiffusive fluxes used to complete the updated solutions for all the hydrodynamic variables.

From a numerical perspective, the most challenging aspect of this simulation has been to develop an algorithm that is robust enough to handle regions of ultralow density. In this simulation we expect ultralow density regions to develop. Where current sheets tear, we will have divergent flows at Alfvénic speeds in an already low density plasma. We will also have the cross section of a flux rope with helical field lines expanding rapidly as it rises through an atmosphere in which the density varies approximately as r^{-5} . In any MHD code these ultralow density regions pose problems associated with the temporal and spatial accuracy of the algorithms discretization and with the assumptions inherent in the nonrelativistic MHD description.

If the density in our numerical solution drops to unphysical ultralow values in regions of strong magnetic field, the Alfvén

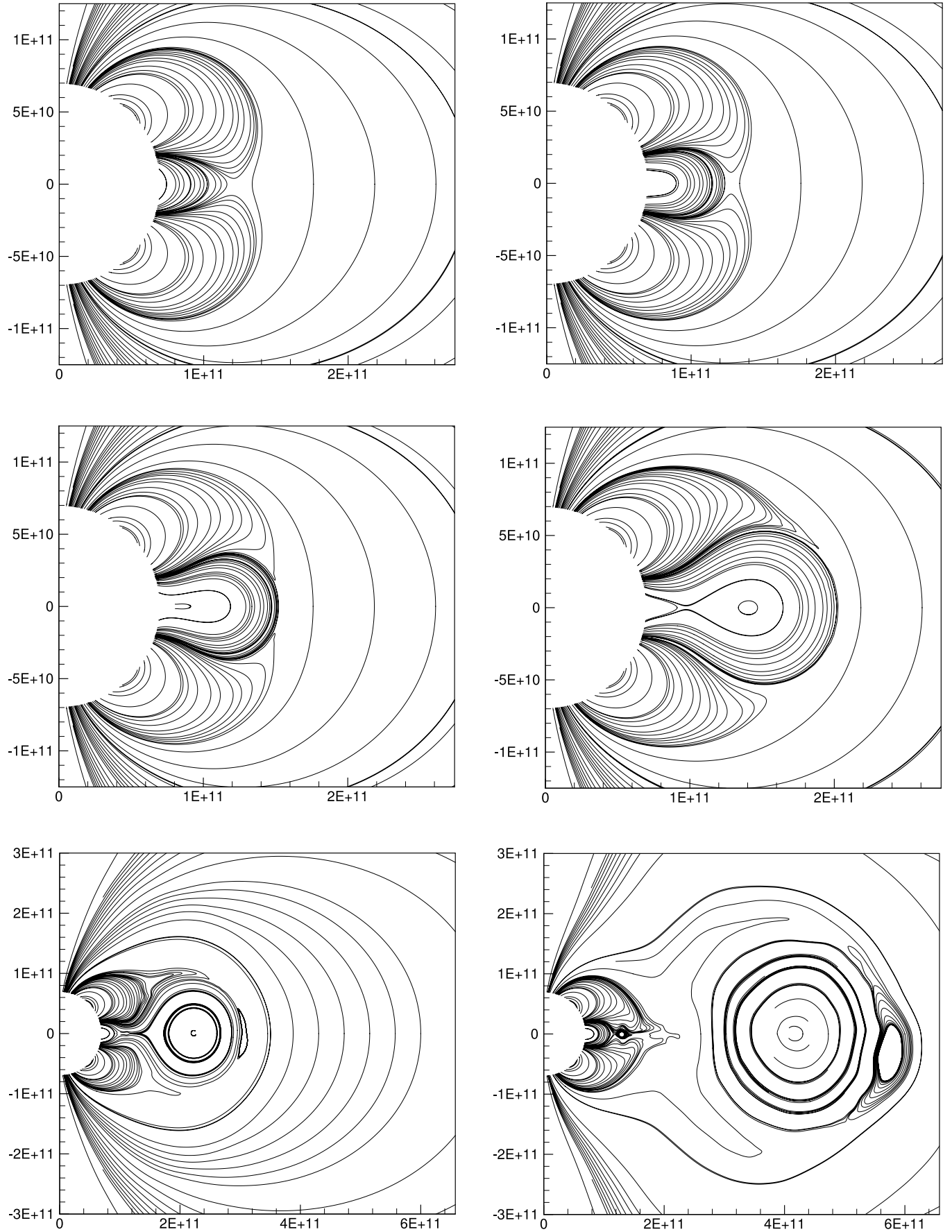


FIG. 1.—Snapshots of selected field lines in the inner region of the computational domain, projected onto the $\phi = 0$ plane. Snapshot times are, from left to right and top to bottom, 0, 50251, 70680, 79008, 85185, and 95020 s, respectively. The spatial scale in the last two frames is expanded to best show the evolving flux rope.

speed can grow to be a significant fraction of the speed of light. To properly model this regime would require a kinetic description with relativistic equations. We would be forced to use such short time steps to achieve stable and accurate solutions that the calculation would be prohibitively expensive. Since we do not believe these high-frequency modes are important in the global evolution of CMEs, we retain a nonrelativistic MHD approximation. However, we modify the momentum equation following an approach pioneered by Boris (1970), commonly known as the “Boris correction.”⁵ The time derivative in the momentum equation is replaced by

$$\frac{\partial}{\partial t}(\rho \mathbf{v}) \longrightarrow \frac{\partial}{\partial t} \mathbf{M}, \quad (5)$$

$$\mathbf{M} = \rho [\mathbf{v}(1 + q^2) - \mathbf{q}\mathbf{q} \cdot \mathbf{v}], \quad (6)$$

with

$$\mathbf{q} = \frac{\mathbf{B}}{\sqrt{4\pi\rho c^2}} = \frac{\mathbf{v}_A}{c}, \quad (7)$$

where \mathbf{v}_A is the Alfvén velocity. As the local Alfvén speed becomes significant in comparison with the speed of light, this has the effect of increasing the inertia associated with the momentum in the direction perpendicular to the local magnetic field. By choosing artificially low values of c in equation (7), we effectively dampen cross-field accelerations in regions of low mass density. In our code we chose a value of $c = 3000 \text{ km s}^{-1}$.

The Boris correction helps to reduce the risk of numerical cavitation. We also follow the standard practice in MHD codes of setting the field-aligned component of the Lorentz force to zero. However, in an ideal MHD code, when rapid reconnection occurs, significant field-line curvature develops on scales close to the grid cell size. Inevitably this leads to errors due to spatial discretization. When these errors occur in regions of low density, the potential for cavitation exists. In our FCT code we conjecture that this potential can be compounded by differences in the phase errors that occur in the solutions to the mass and momentum density equations. In the neighborhood of rapid reconnection, strong Lorentz forces occur in close proximity to regions of divergent flow with low density. If phase errors cause excess momentum to bleed into these low-density regions, the result is excessively large velocities that can drive the evolution of the magnetic field in unphysical ways.

To avoid this problem we have developed a tunable method for additional limiting of the antidiffusive fluxes in the neighborhood of very low densities. The factor by which the antidiffusive fluxes are reduced is multiplied by the function

$$h(r, \theta, t) = 1 - h^*(r, \theta, t), \quad (8)$$

evaluated on the faces of each grid cell. When $h^* = 0$, no reduction in antidiffusion occurs. We set h^* at cell center to be

$$h^* = \begin{cases} \min\left(1, \left[\left(3 - \frac{\rho}{\rho_{\min}}\right)\frac{2}{3}\right]^2\right) & \text{if } \rho < 3\rho_{\min}, \\ 0 & \text{otherwise.} \end{cases} \quad (9)$$

This choice is somewhat arbitrary and is designed to increase smoothly from 0 to 1 as ρ drops below $3\rho_{\min}$ to $1.5\rho_{\min}$. The value of h^* at each cell interface is then computed by averaging the value in the cells on each side of the interface. In addition, we apply a diffusive operator to h^* to spread its influence into the immediate neighborhood, with a diffusion coefficient that is given by $1/(8dt)$. Finally, at the start of each time step we decay the existing value of h^* by 0.125 so that excess diffusion is maintained only as long as it is required.

We set the value of ρ_{\min} to

$$\rho_{\min} = \frac{1}{40} \rho(r, t = 0). \quad (10)$$

This approach is effective in reducing the severity of cavitation events. It is applied to the hydrodynamic variables, but not to the magnetic field. Since the only additional diffusion that the magnetic field will experience is produced through the indirect influence of the extra mass and momentum diffusion, we expect this to be weak.

2.3. Numerical Grid

We assume azimuthal symmetry and consequently solve the MHD equations above in 2.5 dimensions.⁶ The computational domain extends from an inner radial boundary ($1 R_{\odot}$) at the solar surface to the outer radial boundary at $30 R_{\odot}$, and from the north pole $\theta = 0$ to the south pole $\theta = \pi$. In principle the equator represents a symmetry plane in this idealized model, and we could choose to model only one hemisphere. However, we believe there is an important symmetry breaking process in this problem, associated with the development of magnetic islands on the equatorial radius (see § 3.1). This may influence the observed speed of eruption, and so we choose to model the full θ -range.

The numerical grid has a static adaptive refinement superposed on a base grid that is uniformly spaced in the θ -direction. The grid spacing is proportional to r in the radial direction, so that the grid cell aspect ratios are constant and not a function of r . The base grid has a resolution of 128×256 . In the inner regions we have two additional refinement levels as shown in Figure 2. Each refinement level has grid spacing reduced by a factor of 2 over the previous refinement level, so that near the equator on the inner radial boundary the resolution is equivalent to a grid of 512×1024 . The figures in this paper show results from runs with this grid, but for comparison we have also performed simulations with larger and smaller refinement levels.

The nonuniform radial spacing makes the code nominally first-order accurate spatially. However, the second-order error term introduced by the nonuniform spacing has a coefficient whose magnitude is determined by the rate at which the grid spacing changes. In our grids this spacing changes slowly. As a result we believe that the contribution of this error term to the total error is not larger than the contribution from the third-order error terms for the resolution we have used. We have validated the code by substituting a computationally expensive fourth-order spatial interpolation function where appropriate, to make the code formally third-order accurate, and

⁵ The code used by Antiochos et al. (1999) employed a version of the Boris correction that had no dependence on the local field direction.

⁶ The variables $\rho, \mathbf{v}, U, \mathbf{B}$ are functions of r and θ , but not ϕ since $\partial/\partial\phi = 0$, but the vectors \mathbf{v}, \mathbf{B} can have nonzero components in the ϕ -direction.

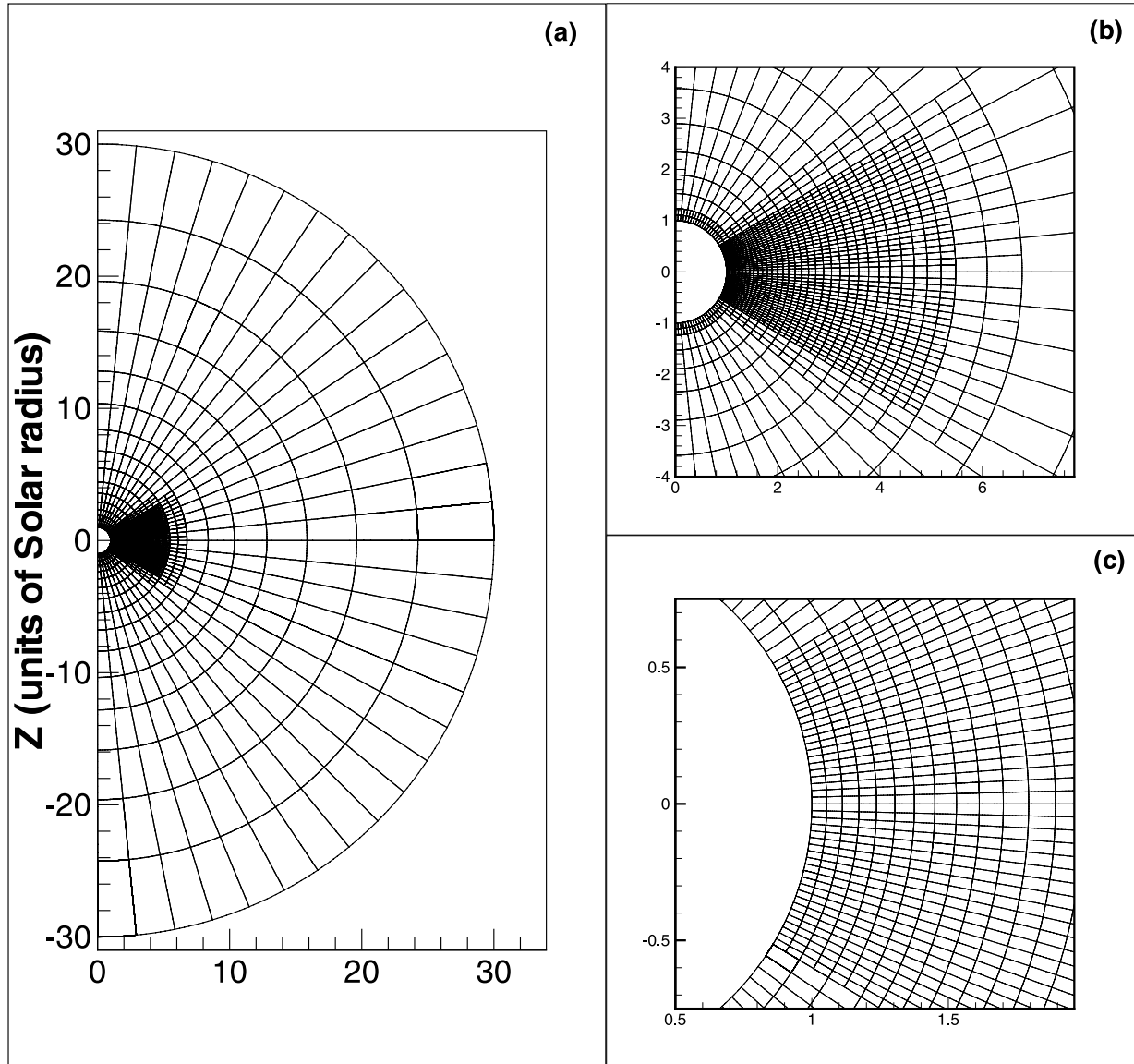


FIG. 2.—Grid used for this computation. Each box represents a block of 8×8 grid cells. Frame (a) is the complete grid, while (b) and (c) show successively more enlarged views of the inner equatorial region of the grid.

have shown that this makes no significant qualitative difference to our results at the resolution of our current grid.

2.4. Initial Conditions

The initial magnetic field is potential and consists of a combination of dipole and octopole components. Because of the azimuthal symmetry, it is easily expressed in terms of Euler potentials,

$$\mathbf{B} = \nabla\alpha(r, \theta) \times \nabla\phi, \quad (11)$$

where we choose

$$\alpha(r, \theta) = \sin^2\theta \frac{R_\odot}{r} + (3 + 5 \cos 2\theta) \sin^2\theta \frac{R_\odot^3}{2r^3}. \quad (12)$$

This form for the flux function α produces a field with four distinct flux systems as shown in Figure 1. At large radius the

field is dominated by the dipole component. Near the solar surface there is an inner flux system centered on the equator, bounded at higher and lower latitudes by two additional flux systems. There is a null point at a radius of $r = \sqrt{3} R_\odot$, and the field lines passing through this point define separatrices bounding the four flux systems.

Since the initial numerical magnetic field only samples the analytic potential solution, the numerical Lorentz force will be approximately zero, but not exactly zero. Therefore, we subtract this small numerical Lorentz force associated with our initial field from the time-dependent Lorentz force evaluated during the simulation. As a result, the initial field is a true equilibrium of our modified algorithm and does not evolve until we perturb it.

The initial mass density is computed as a solution to the equation of hydrostatic equilibrium, with a temperature profile given by

$$T(r) = T_\odot \frac{R_\odot}{r} \text{ K}, \quad (13)$$

and consequently an initial density profile of

$$\rho(r) = \rho_{\odot} \left(\frac{R_{\odot}}{r} \right)^{1-\mu}, \quad (14)$$

with $\mu = 2k_B T_{\odot}/g_{\odot}$, where $T_{\odot} = 2 \times 10^6$ K is the temperature, $\rho_{\odot} = 2 \times 10^8 m_p \text{ g cm}^{-3}$ is the mass density, and $g_{\odot} = 2.7 \times 10^4 \text{ cm s}^{-2}$ is the gravitational acceleration at the inner radial boundary.⁷ The temperature and density profiles are chosen so that the plasma β in the model is small, in agreement with the real corona. For the form of α given above, we find that at the solar surface the magnetic field strength is 2 G at the equator and 10 G at the poles, which yields a value for β varying from 0.5 to 0.02 at the poles. The values for β along a radial line at the equator and at 45° are shown in Figure 3. Of course the β diverges at the magnetic null, but we note that along the mid-latitude line, β remains smaller than unity out to large radius.

2.5. Boundary Conditions

At the inner radial boundary (R_{\odot}), we enforce a line-tied condition on the magnetic field. This boundary is also assumed to be impenetrable. More precisely, these conditions are imposed by setting

$$\frac{\partial B_r}{\partial t} = 0, \quad (15)$$

$$v_r = 0 \quad (16)$$

on the boundary.

The system is driven by imposing a shear velocity profile in the ϕ -direction on the inner boundary. The shear is applied in a narrow region centered about the equatorial neutral line. The velocity is antisymmetric about the equator with a latitudinal dependence given by

$$v_{\phi} = \begin{cases} 0 & \text{if } |\psi| > \Theta, \\ V_0(\psi^2 - \Theta^2)^2 \sin \psi & \text{if } |\psi| \leq \Theta, \end{cases}$$

where $\psi = (\pi/2 - \theta)$, $\Theta = \pi/15$ defines the latitudinal extent of the shear region on each side of the equator, and the shearing amplitude $V_0 = 8682.52 R_{\odot}(\pi/2)$. The shearing is applied with a sinusoidal time profile of period 2τ and is imposed for a half cycle of the sinusoid, i.e., for a time interval of $\tau = 100,000$ s. As a consequence of this shear, the maximum angular displacement in azimuth of a field line footpoint at the photospheric boundary is $\pi/2$, which implies a maximum velocity less than 10 km s^{-1} and an average shear velocity considerably less. From Figure 3 we note that in our model corona the Alfvén speed can exceed 300 km s^{-1} , which indicates that although our system is not driven as slowly as the real corona, it is still driven quasi-statically. It should be emphasized that the photospheric shear assumed in our model is merely a convenient method for driving the system; it is not meant to represent the process by which a real filament channel forms. Flux emergence is likely to play a major role in the formation process, but modeling flux emergence in a coronal simulation is very difficult computationally. As long as the system is driven quasi-statically, we do not expect the detailed process by which the shear forms to have a significant

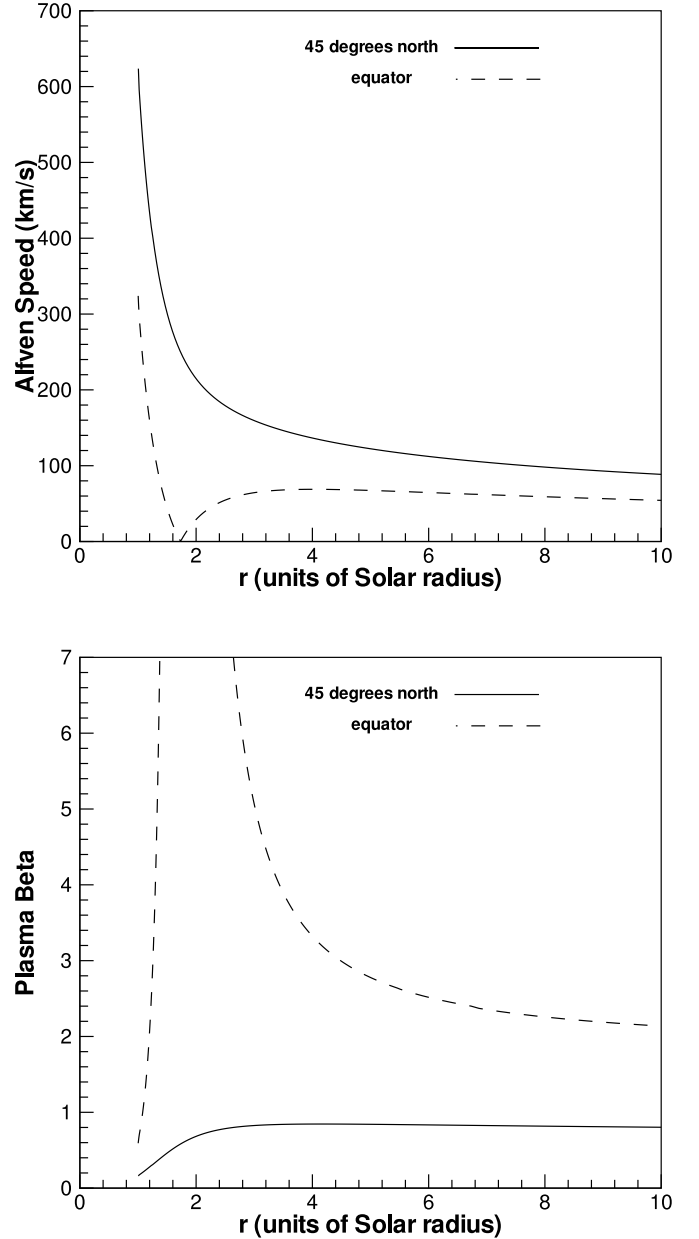


FIG. 3.—*Top*: Alfvén speed as a function of radius at $t = 0$, along the equatorial radius and along a radial line at 45° north. *Bottom*: Plasma β along the same radial lines.

effect on the eruption dynamics, at least, in the breakout model.

In these simulations we attempted to place the outer radial boundary as far out as computationally possible, $r = 30 R_{\odot}$, so that it would have a negligible effect on the eruption structure and evolution. As seen below, the eruption is well into its decay phase before the shock or the ejected plasmoid reaches the outer boundary. Open boundary conditions are imposed there. At the polar boundaries, the boundary conditions are determined from the azimuthal symmetry constraint.

3. RESULTS

3.1. Evolution of Velocity and Energy

The evolution extends the initial results obtained by Antiochos et al. (1999). The field and plasma evolution is illustrated in a sequence of snapshots shown in Figures 1, 4, 5, and 6.

⁷ This density is twice the base density used by Antiochos et al. (1999).

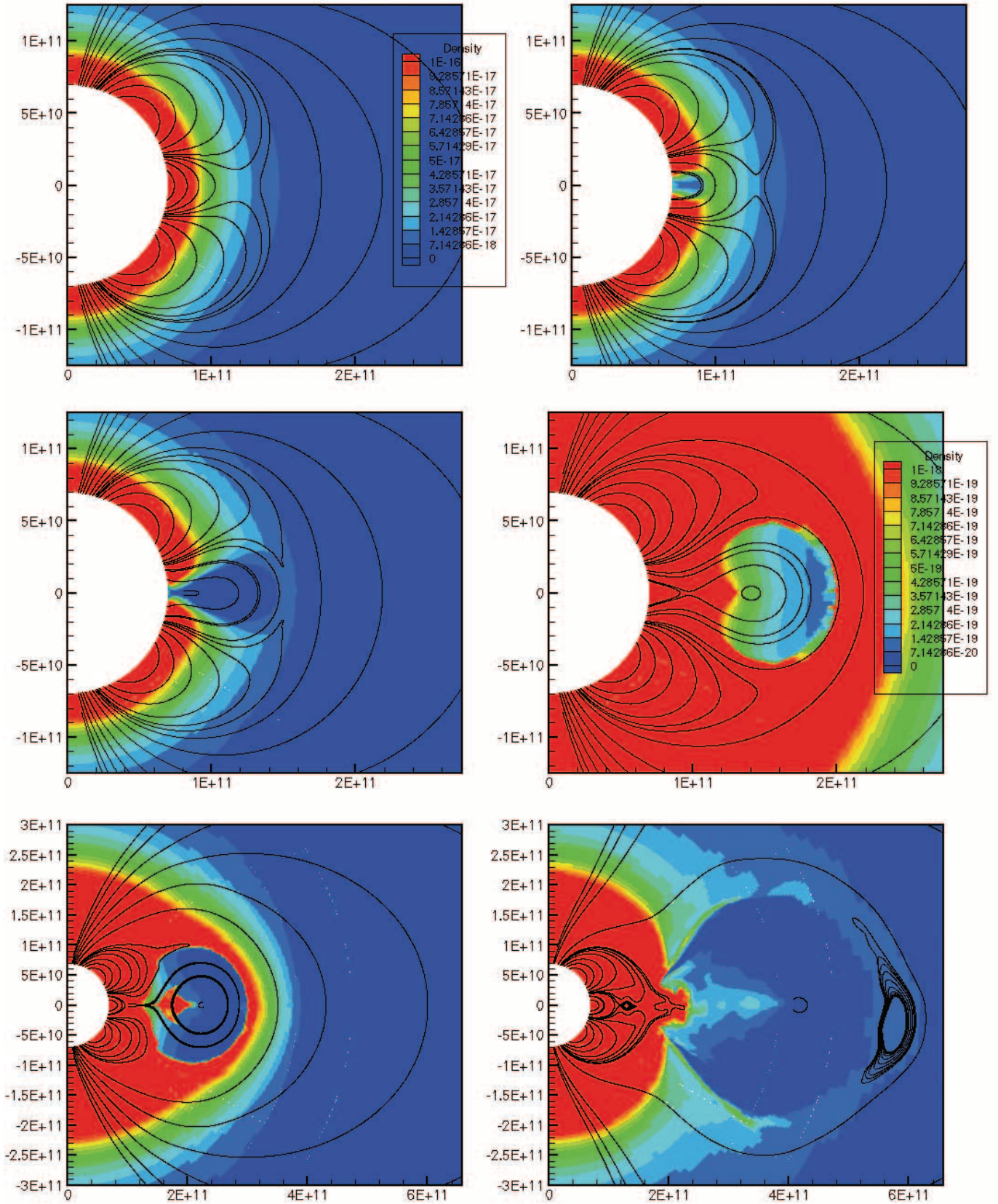


FIG. 4.—Mass density for the frames shown in Fig. 1. The color map represent mass density in units of g cm^{-3} . Some field lines are superposed to help compare features in the color map with the corresponding features in the field-line plots. Note that the color map scale is modified in the last three frames to highlight diffuse structure in the expanding flux rope.

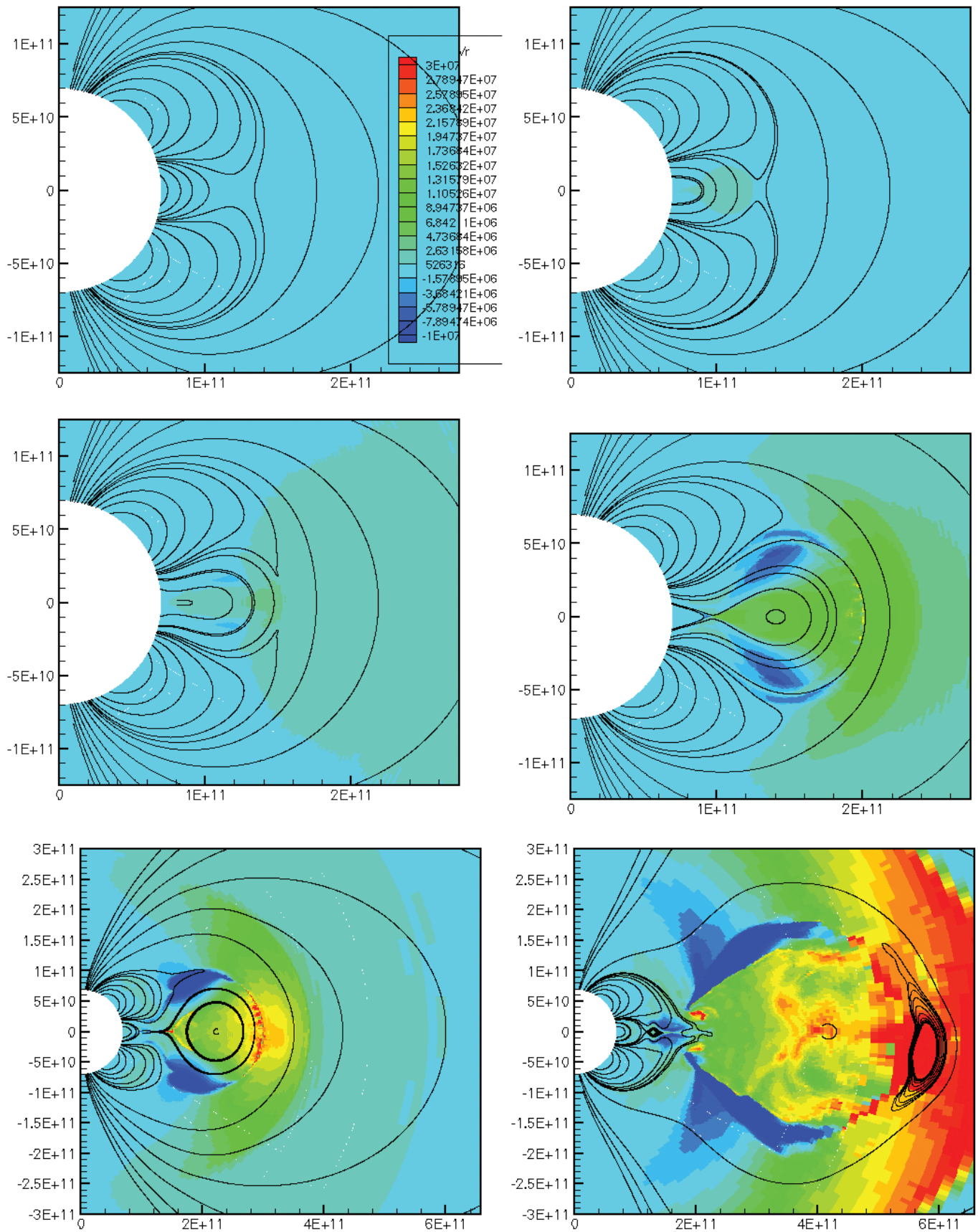


FIG. 5.—Same as Fig. 4, except the color map represents radial velocity in cm s^{-1} .

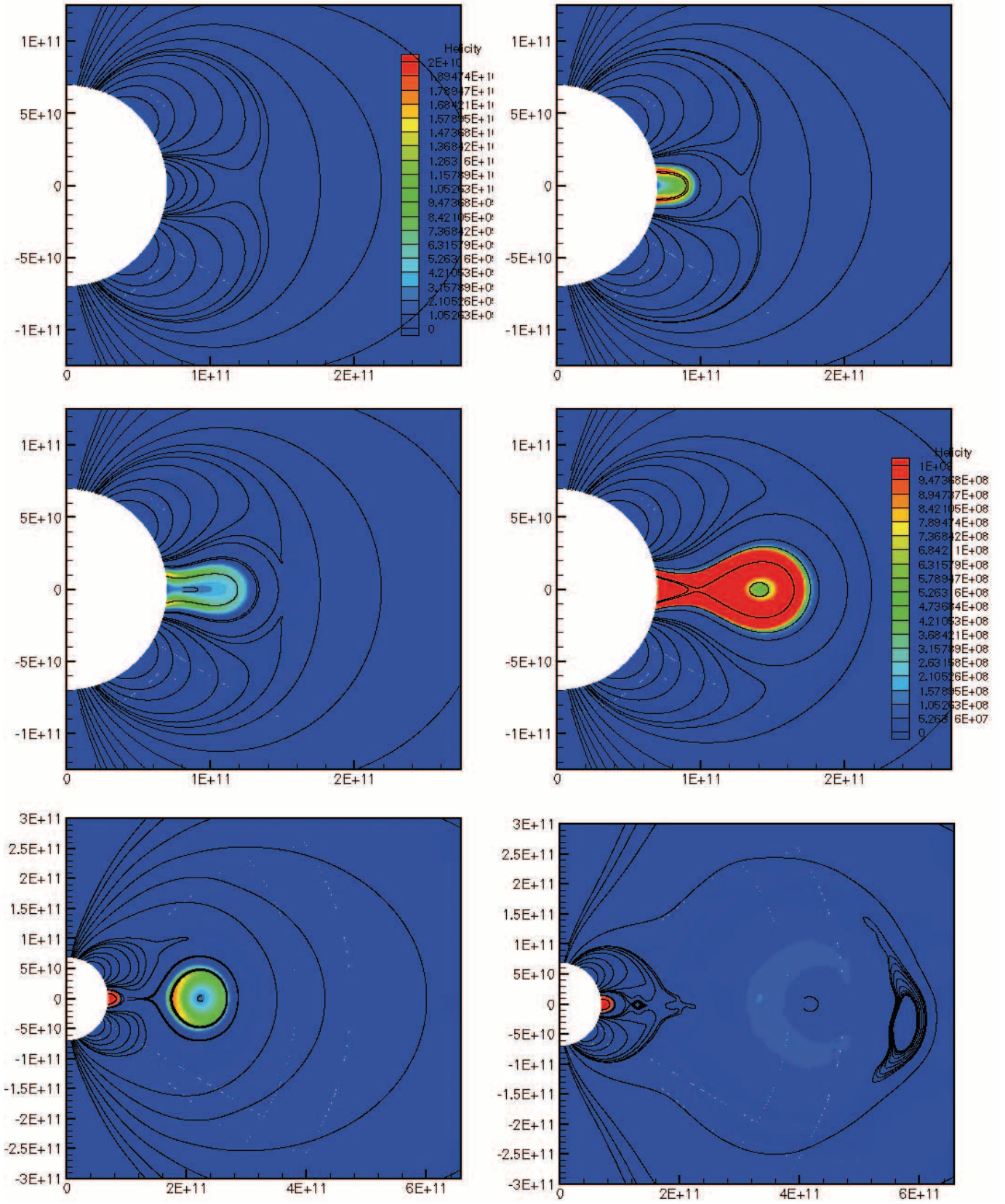


FIG. 6.—Same as Fig. 4, except the color map represents helicity density. Note that the color map is altered for the last three frames to highlight the lower helicity densities in the expanding flux rope.

Figures 4–6 show the evolution of the field superposed on color density maps of the mass density, radial velocity, and helicity, respectively. Note that the field lines in our model are three-dimensional objects, since we solve for all three components of \mathbf{B} . To display them here we project them onto a single plane, by plotting every point along each three-dimensional field line, not at its true location (r, θ, ϕ) , but instead at $(r, \theta, 0)$. The field lines in these figures have been drawn by choosing a set of starting points in the $\phi = 0$ plane and tracing the field lines (in both positive and negative directions) beginning at each of those points. We selected starting points on the inner boundary and at points along the equatorial radial axis. Some field lines are terminated prematurely if they extend beyond the range $-\pi/4 < \phi < \pi/4$, or after they have accumulated 3000 arc segments, to avoid clutter. When comparing the frames at different times, it should be kept in mind that only those field lines that are traced from starting points on the inner boundary are the “same” in the different frames and therefore show the motion of a particular field line (assuming the evolution is ideal). In order to show the plasmoid with disconnected field lines that forms, we also use starting points along the equatorial radius. Since these points are fixed in space, the field lines traced from these points are not the same in the different frames, but they can be used to illustrate the general position of the plasmoid.

It is evident from Figure 1 that as the inner flux system is stressed it expands outward, pushing up against the overlying field that inhibits its expansion. The X-point between the two systems deforms into a current sheet elongated in the θ -direction. When the thickness of this current sheet reaches the grid scale, the effects of numerical diffusion become significant and the two systems begin to reconnect. We will refer to this reconnection as the “breakout” reconnection. Field lines at the outer edges of the inner flux system reconnect with overlying field and subsequently snap back to join the inner mid-latitude flux systems, allowing the remaining inner flux system to expand further outward. As a result of the large outward expansion, the field lines deep in the inner system begin to approach an open geometry, and hence a radial current sheet develops there. Again, when the current sheet thickness becomes of order the grid scale, diffusion becomes significant and reconnection sets in. We will refer to this as the “flare” reconnection. The flare reconnection produces a disconnected flux rope (plasmoid) between the inner and outer flux systems, which continues to rise. The plasmoid eventually escapes from the system, and the inner field relaxes back to a configuration that is similar in general features to its original configuration but with much less shear. We emphasize that the flare reconnection and the production of a disconnected flux rope are certainly not unique to the breakout model. They are an inevitable consequence of eruption and are well-known features of essentially every 2.5-dimensional model (e.g., Mikić & Linker 1994).

Another feature that is evident in Figure 1, especially in the late stages of the eruption, is the appearance of a large magnetic island in front of the ejected plasmoid. The origin of this island is the artificial symmetry in the simulation. When the breakout current sheet becomes sufficiently extended in the θ -direction so that its length-to-width ratio begins to exceed a factor of 10 or so, magnetic tearing occurs, causing the sheet to break up into multiple islands (Furth et al. 1963). Island formation is a ubiquitous feature of 2.5-dimensional reconnection, especially in simulations with high spatial resolution so that long current sheet can develop (e.g., Karpen et al. 1996; Shibata et al. 1992). Note that in our simulation, magnetic islands also form in the flare current sheet along the radial

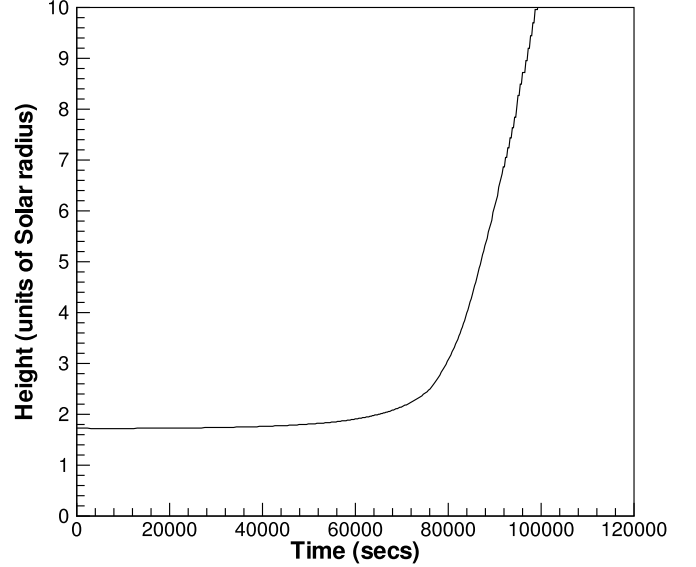


FIG. 7.—This plot tracks the extremum in the radial integral of the flux of B_θ across the equator, corresponding to the location of the outer X-point.

direction. But these islands are short-lived and remain small because they rapidly migrate either up or down along the radial current sheet and merge with the inner or outer flux systems. We expect that, in reality, islands forming in the breakout current sheet would also be short-lived, but the mathematical problem that we solve has a symmetry plane at the equator, with $\rho, p, U, v_r, B_\theta, B_\phi$ symmetric and v_ϕ, B_r antisymmetric with respect to reflection in the equatorial plane. If an island forms that is centered about the equator, as is almost certain to occur, then because of the equatorial symmetry such an island cannot move either up or down along the current sheet and disappear. An equatorially symmetric island can only grow indefinitely. Note that such an island chokes off the breakout reconnection by converting the X-point to an O-point. All the mass and field accumulated in the island must be ejected outward along with the plasmoid; hence, the island slows down the eruption. By simulating the full θ -range rather than only a single hemisphere, as discussed in § 2.3, we break the symmetry numerically and mitigate these effects. Islands form almost immediately in the breakout current sheet, but early in the eruption they are small and there is enough numerical asymmetry present to move them up or down. It is only in the late stages when the ejection is moving near the Alfvén speed that a large persistent island forms.

The critical issue for any CME model is the speed of the eruption. To account for fast CMEs, the ejection speed must be of order the Alfvén velocity. Furthermore, since all numerical simulations have effective resistivity orders of magnitude higher than the solar value, any viable CME model must predict a negligible dependence of ejection speed on the Lundquist number. In order to determine the ejection speed in the simulation, we define the leading edge of the eruption to be the position of the X-point ahead of the plasmoid. This quantity is shown as a function of time in Figure 7. Since B_θ changes sign at the null, we can accurately obtain the position of the X-point by calculating the location of the outermost extremum in the radial integral of the B_θ flux through the equatorial plane,

$$\int_{R_\odot}^r B_\theta(r', \theta, t) r' \sin \theta dr'. \quad (17)$$

TABLE 1
UPPER X-POINT POSITION AND SPEED AT TIME OF MAXIMUM VELOCITY

Maximum Resolution	Radius (R_{\odot})	Velocity (km s^{-1})
256×512	3.6	170
512×1024	4.3	233
1024×2048	4.4	233

NOTE.—Data refer to time 85,000 s in each case.

This procedure has the added advantage of taking into account the fact that the X-point changes to an O-point late in the evolution.

As the inner flux system expands, the X-point moves outward at a speed determined by the slope of this curve. Just before the plasmoid pinches off because of the onset of flare reconnection, this slope indicates an expansion speed of 50 km s^{-1} . Once the flux rope pinches off, at about 73,000 s, the outer X-point accelerates rapidly, reaching an “ejection” speed of 365 km s^{-1} before it reaches the outer limit of our simulation. Almost all the acceleration occurs below $3 R_{\odot}$. For comparison, the Alfvén speed at the equator at $3 R_{\odot}$ before the flux rope arrives is 65 km s^{-1} , and at 45° north it is 160 km s^{-1} (Fig. 3). As the plasmoid moves outward, it creates a density enhancement around it as it sweeps up coronal material (Fig. 4). Since the plasmoid is moving at supersonic and super-Alfvénic speeds, a magnetoacoustic shock forms at the leading edge of this enhancement (Fig. 5). These results verify that, at least for this simulation, the breakout model does produce a fast CME.

In order to determine the dependence on resistivity, we have run identical simulations but with refinement levels one lower and one higher than that shown in Figure 2, corresponding to effective grids of 256×512 and 1024×2048 , respectively. Grids larger than 1024×2048 are too CPU intensive to run in reasonable times, and as will be discussed in § 3.3 grids smaller than 256×512 are too inaccurate. The evolution is qualitatively identical for all cases, with a plasmoid ejection as in Figures 1–5. For quantitative comparison, Table 1 lists the position and velocity of the outer X-point at approximately 85,000 s when the eruption is fully developed and is approaching its maximum velocity. It is evident that the speed does not decrease with refinement level; in fact, it exhibits a significant increase between the first and second case and a small increase between the last two cases. We believe the primary reason for this increase is that a larger grid implies a smaller effective resistivity, and consequently, the system can build up more free energy before it begins to reconnect. As is evident from Figure 1, the onset of breakout reconnection and the ejection of the plasmoid occurs well before the end of the shearing phase, at $t = 100,000 \text{ s}$. Delaying the eruption implies that it will release more free energy and therefore have higher initial acceleration. Of course, the maximum velocities in the system are limited by the Alfvén speed, and it appears that the last two refinement cases are approaching this limit.

Another important issue for all models is the energetics of the eruption. The fast ejection speed in our simulation implies that the kinetic energy should play a major role. Figure 8 shows the evolution of several important energy terms in the system. Since the system is driven by the shear flow in the azimuthal direction, the bulk of the free energy is stored in the azimuthal field, B_{ϕ}^2 . The azimuthal energy rises smoothly, reaching a maximum at around 65,000 s, and then begins to decrease because of the onset of outward expansion, even though the

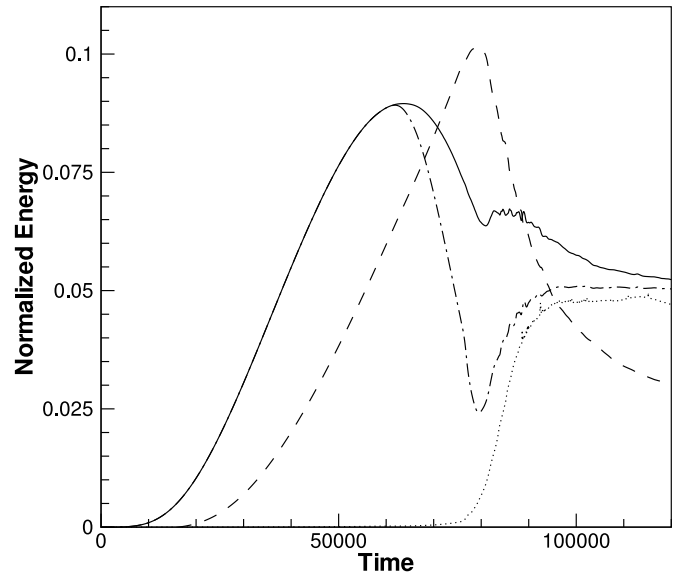


FIG. 8.—Energy components as a function of time. The lines represent azimuthal magnetic energy (solid line), the azimuthal magnetic energy below $1.5 R_{\odot}$ (dash-dotted line), the change in nonazimuthal magnetic energy from the original field (dashed line), and the kinetic energy (dotted line). The units of energy are ergs divided by the volume R_{\odot}^3 .

shearing continues on until 100,000 s. Between 65,000 and 80,000 s the free energy in the nonazimuthal components, $B_r^2 + B_{\theta}^2$, rises rapidly, implying that the energy is being transferred from the azimuthal to nonazimuthal components of the field. This time period corresponds to the creation of the radial current sheet deep in the inner flux system and to the onset of reconnection there. From 80,000 to 90,000 s, the nonazimuthal field decreases sharply, corresponding to a steep rise in kinetic energy. We note that the kinetic energy accounts for approximately half the energy lost by the field. The rest is taken up primarily by the increase in gravitational energy, and to a lesser extent by internal energy at the current sheets and shocks. Since not all the azimuthal field is injected into the plasmoid—a fraction remains in the closed field region that does not erupt—we also show in Figure 8 the azimuthal magnetic energy below $1.5 R_{\odot}$. Comparison of the total azimuthal energy with that below $1.5 R_{\odot}$ indicates that by the end of the simulation, 120,000 s, almost all the azimuthal magnetic energy in the ejected plasmoid has been lost because of the plasmoid’s large expansion.

3.2. The Rapid Acceleration Phase

In Figure 7 we see that the outward radial expansion of the sheared flux is slow and gradually accelerating at first but begins a period of rapid acceleration around 70,000 s. What triggers this rapid acceleration phase?

The first point to recall is that, since we solve the ideal equations, the resistivity in our calculation is numerical, which means that it is strongly scale-dependent. For regions where the gradients in magnetic field are well resolved, scale lengths greater than 10 grid points, the effective Reynolds number is of order 10,000 or higher. But once the scale lengths decrease to the size of a few grid points, or less, the effective Reynolds number becomes of order unity. We expect that on the real Sun a similar situation holds in that once a coronal current sheet becomes strong enough, some current-driven instability or kinetic effect kicks in, increasing the effective resistivity. Hence, the trigger mechanism for the eruption in our simulations is the

onset of reconnection at the upper null due to the turn-on of a large numerical resistivity, but in fact such a clear-cut trigger may not be necessary for the model.

At the start of our simulations the magnetic field is potential and the scale for the gradients at the coronal null is large, tens of grid points. But as the neutral line shear increases, the coronal field expands outward, deforming the field at the null. As discussed in Antiochos et al. (1999), the scale at the null (width of the currents there) decreases inversely with the radius of the null point (amount of expansion). We find that as long as the magnetic scale at the null is large compared to the grid size, there is no measurable reconnection (on the timescale of the runs). The system appears to be in a stable equilibrium with no evidence for either instability or loss of equilibrium. This is true even if the energy in the field increases to a value well above the minimum open field energy. It should be emphasized that such a stable energy buildup phase is necessary for any fast CME model to be viable.

But as the shearing continues, the width of the current structure at the null eventually drops to the grid scale and reconnection begins. Once reconnection appears, we find that the expansion simply runs away, even if one stops the shearing at this point. This result is the motivation for our argument concerning the feedback mechanism.

One could claim that the trigger mechanism in our model is actually the “turn-on” of numerical resistivity due to its grid dependence, and for our particular calculation this is certainly justified. (It may also be the case for the real Sun). But we question whether such an abrupt turn-on of resistivity is really necessary for the model to operate.

Even if the resistivity were constant and independent of grid scale, the magnetic diffusion rate would still have a strong scale dependence (varying as the square of the scale); therefore, it is likely that one would still obtain an evolution similar to that described above. For small shear the rate of reconnection at the null would be negligible compared to the rate of shearing and expansion, so that one would still have a stable energy buildup phase. Furthermore, one would expect the scale at the null point to decrease with expansion until eventually the rate of reconnection there became significant compared to the ideal evolution rates. The critical question is how the reconnection affects the subsequent evolution. The ongoing reconnection continually acts to drive the system further out of force balance, which accelerates the rate at which the flux tries to move through the X-line (including also the lower X-line, once it appears). Thus, as long as some finite resistivity is present, a feedback occurs that rapidly accelerates the outward expansion. Consequently, we expect that even with a constant resistivity, the evolution of the null point would resemble that shown in Figure 7, in that one should see a nearly non-reconnecting, linear expansion phase followed by an exponentially increasing expansion phase, but probably with a less abrupt turnover from linear to exponential. If so, then the key feature of the model is the positive feedback between reconnection and expansion, not the fact that the resistivity has a sharp turn-on. On the other hand, there is no doubt that the use of numerical resistivity in the present simulations helps define a clear trigger to the eruption.

The lower X-line appears and a flux rope begins to form at about the same time as the onset of rapid outward expansion. It might be argued that this timing indicates that the rapid expansion phase is due to a loss of equilibrium, rather than the reconnection feedback mechanism. A loss of equilibrium has been seen in a number of flux rope studies and is the trigger

mechanism for the flux cancellation models. If true, this would bring the flux cancellation and breakout models into a common physical framework. However, while we recognize that this simulation does not answer the question definitively, we doubt that a loss of equilibrium is operating in our simulations, because the system begins its rapid outward expansion well before a substantial plasmoid forms. By 73,000 s, when the lower X-line first appears, the system has already entered its rapid acceleration phase, and a substantial plasmoid is not present until around 80,000 s, at which time the eruption is near its final velocity.⁸ In the flux cancellation models, equilibrium is lost only after the plasmoid contains a substantial amount of flux. For example, in the recent paper by Lin et al. (2004), these authors estimate that the initial stable, preeruption flux rope contains roughly half the ejected flux. Of course, this fraction will depend on the particular magnetic configuration, but it seems inevitable that in order for a flux rope to produce a loss of equilibrium, the rope must contain a significant fraction of the flux in the system. This is not true for our simulations.

3.3. Evolution of Helicity

The role of helicity in CMEs has received considerable attention in recent years. Several authors have argued that CMEs are the primary mechanism by which the Sun sheds excess helicity and toroidal flux, and consequently, CMEs may play a key role in the solar cycle (e.g., Bieber & Rust 1995; Kumar & Rust 1996; Low 2001; Rust 2001; Demoulin et al. 2002; Nindos et al. 2003; Gopalswamy et al. 2003). It is important, therefore, to understand the evolution of helicity in models of CME initiation such as breakout. We can investigate this question in detail with our simulations.

Since the solar surface does not represent a flux surface, the helicity

$$K = \int \mathbf{A} \cdot \mathbf{B} dV \quad (18)$$

is not conserved in ideal MHD. However, the relative helicity (Berger & Field 1984; Finn & Antonsen 1985),

$$K_r = \int (\mathbf{A} + \mathbf{A}_p) \cdot (\mathbf{B} - \mathbf{B}_p) dV, \quad (19)$$

is conserved, where \mathbf{B}_p is the potential field with the same flux distribution through the surfaces bounding the computational domain as \mathbf{B} . If we choose \mathbf{B}_p to be the initial potential field given by equations (5) and (6), then this condition is satisfied, since our line-tying boundary condition at the solar surface requires that \mathbf{B}_r not change with time. Under conditions of azimuthal symmetry, the helicity density can be written as (Antiochos et al. 2002)

$$k_r(r, \theta, t) = 2A_\phi B_\phi, \quad (20)$$

so the total relative helicity at time t is given by

$$K_r = \int k_r(r, \theta, t) dV. \quad (21)$$

⁸ The magnetic flux crossing the equator between the inner X-line and the center point of the flux rope is 2.1×10^{21} G cm² at 75,000 s, or 9% of the total of 2.3×10^{22} G cm² in the original inner flux system. By 80,000 s this rises to 5.1×10^{21} G cm² (22%), and by 82,500 s it reaches 9.3×10^{21} G cm² (40%).

In Figure 6 we show the distribution of helicity density at various stages in the evolution of the system. The helicity shed by the ejection of the plasmoid represents approximately 80% of the total originally injected into the system. This result suggests that although CMEs remove the bulk of the coronal helicity, a significant fraction remains behind, which implies that some other mechanism operating in the corona itself must be responsible for dissipating the rest of the helicity. There are several caveats, however, to this conclusion, the main one being that in our simulation we consider only the helicity associated with the neutral line shear. This limits all the helicity carried off by the ejected plasmoid to be contained in an inner core region of the plasmoid comprised of the sheared field. In the real corona there is likely to be considerable helicity associated with large-scale magnetic fields because of the effects of differential rotation (DeVore 2000) and active region motions on a global scale. If this overlying field opens up during the eruption, then it will lose essentially all its helicity, and the fraction of coronal helicity carried away by a CME could be substantially greater than 80% of the pre-eruption value.

3.3.1. Influence of Spatial Resolution

The helicity density is a useful quantity for investigating not only the physics of the eruption but also the numerics of the simulation. Since we do not solve an equation for the evolution of helicity density, we can use this quantity as a stringent error measure for the calculation. The rate at which relative helicity is injected into the model at the solar surface is given by the surface integral

$$\frac{dK_r}{dt} = -2 \int B_r A_\phi v_\phi dS, \quad (22)$$

where dS is an element of the surface.

Based on Taylor's conjecture (Woltjer 1958; Taylor 1974; Berger 1984), we expect the relative helicity to be conserved to a good approximation, because the reconnection caused by numerical diffusion occurs in only a small fraction of the simulation volume. If we compare the time integral of the helicity injection rate with the volume-integrated relative helicity density, we can check whether this is the case. These quantities are compared in Figure 9, which shows that at the resolution of our calculation, helicity is well conserved even during the strong reconnection and eruption phase. This test is highly sensitive to the spatial resolution. For the same simulation on a grid of 256×512 points we found that helicity was misconserved by 20%, and on a grid of 128×256 points helicity was misconserved by more than 50%. The ultrahigh resolution 1024×2048 run showed an even better agreement between injected and measured helicity than in Figure 9. These results indicate that a grid of 512×1024 is an optimal resolution for the simulation. Larger grids do not add significantly more accuracy, whereas smaller grids start to degrade the calculation noticeably. Figure 9 also demonstrates the robustness and low diffusivity of our code and the advantages of using an adaptive mesh for physical systems in the breakout model where we expect current sheets to form in only a few locations.

4. DISCUSSION

We have presented in this paper the first simulations of a complete breakout CME. These calculations have allowed us

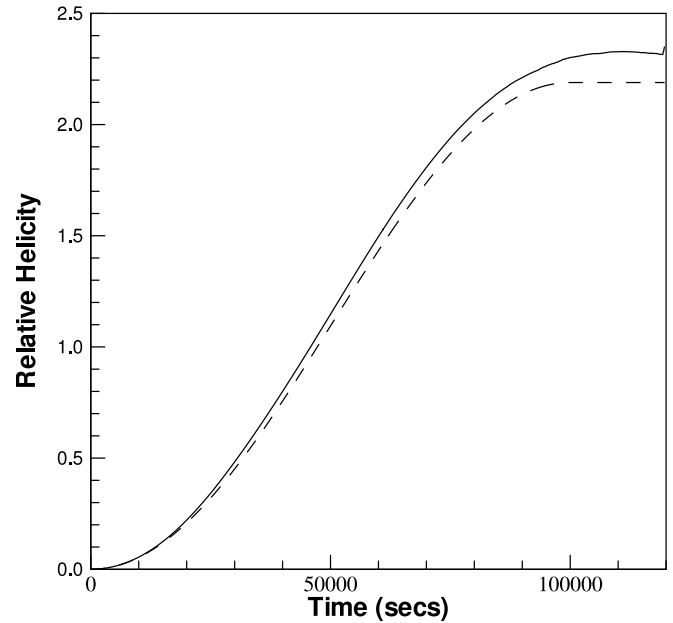


FIG. 9.—Total relative helicity (solid line) in units of $10^{10} R_\odot^3$ as a function of time, compared with the time integral of the injection rate of relative helicity (dashed line).

to answer a number of major questions concerning the eruption. The most important result concerns the speed of the eruption. We find that the model does indeed produce fast CMEs with ejection velocities of order the Alfvén speed. Even more important, the ejection speed does not appear to be sensitive to the refinement level of the calculation, i.e., to the effective resistivity, at least, for a resistivity with a spatial scale dependence similar to that of numerical resistivity. These two conclusions show that the breakout model efficiently converts the free magnetic energy stored in the system to kinetic energy. One caveat, however, is that the simulations presented here are only 2.5-dimensional, whereas a real CME is fully three-dimensional. There will clearly be major differences between three-dimensional and 2.5-dimensional calculations; in particular, a disconnected flux rope will not form in three-dimensional. But the underlying topology of a multipolar flux system with null points in the corona remains unchanged in three dimensions (e.g., Antiochos 1998; Aulanier et al. 2000); therefore, we believe it likely that many of the important results in this paper, such as ejection speed and the general evolution shown in Figures 1–5, are likely to remain valid in three-dimensional geometries.

Another important result of the simulations is that although most of the helicity in the system is ejected during eruption, a significant fraction remains in the corona. In fact, this result is to be expected. It is well known observationally that neutral-line shear does not disappear during an eruptive flare (e.g., Wang et al. 1994). CMEs may be responsible for most of the helicity loss of the corona, but it seems clear that some other mechanism, possibly small-scale diffusion, eliminates the remaining neutral line shear. This conclusion raises the interesting question as to whether CMEs are essential for eliminating coronal helicity, as has been argued by numerous authors.

The work presented here also raises interesting questions concerning observational tests of the breakout model and the implications for CME/eruptive flare prediction. The most convincing observation would be to detect evidence of breakout reconnection before a CME and the accompanying flare.

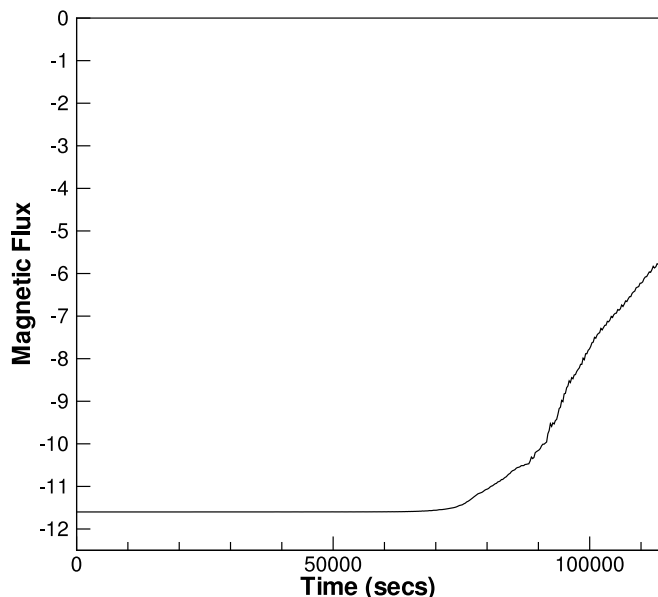


FIG. 10.—Integral of B_θ flux across the equator from the inner boundary to the location of the X-point, plotted as a function of time. The curve is normalized such that -1 is the total B_θ flux across the equator between the inner and outer boundaries.

A critical question therefore is the amount of breakout reconnection that one would expect to observe before CME and flare onset. The answer can be obtained from Figure 10, which plots the total flux below the outer X-point as a function of time. It is evident that by the end of the simulation, approximately half of the original flux overlying the sheared neutral line has been removed by breakout reconnection. The key point is that most of this reconnection occurs after 80,000 s, i.e., after the rapid acceleration (Fig. 7) and the flare reconnection (Fig. 1) have clearly started. We emphasize, however, that even though the

bulk of the breakout reconnection occurs during what would be observed as the eruption/flare itself, this reconnection is essential for the event to take place. As discussed in Antiochos et al. (1999), the sheared field configuration does not have enough energy to open up the overlying restraining field. This restraining field must be moved out of the way by reconnection.

The implications of our results for observations are that the strongest signatures of breakout are likely to be present during the flare impulsive phase. In retrospect, this finding is not surprising. Breakout reconnection is driven by outward expansion of the field and hence will be strongest during the CME rapid acceleration phase when the outward expansion is largest. But a large outward expansion will inevitably produce a current sheet below the erupting flux, which will drive flare reconnection there. In fact, our analysis of the 1998 July 14 eruptive flare showed exactly this behavior (Aulanier et al. 2000). In that event, there was clear evidence of breakout reconnection before flare onset, but the most pronounced signatures were observed during the flare impulsive phase. Our results on the relative timing of breakout reconnection, CME acceleration, and flare onset also appear to be in agreement with recent observations by Zhang et al. (2001) and Gallagher et al. (2003), who find that flare-associated CMEs have a slowly rising initiation phase, followed by a fast acceleration phase roughly coincident with the flare impulsive phase. With further data analysis and theoretical modeling, especially in three dimensions, it should be possible to determine whether this CME initiation phase and rapid acceleration are due to magnetic breakout.

This work was supported in part by NASA, NSF, and ONR. We would also like to thank the referee, whose insight and attention to detail prompted us to clarify our discussion of some key issues.

REFERENCES

- Aly, J. J. 1984, *ApJ*, 283, 349
 ———. 1991, *ApJ*, 375, L61
 Amari, T., Luciani, J. F., Mikić, Z., & Linker, J. 2000, *ApJ*, 529, L49
 Antiochos, S. K. 1998, *ApJ*, 502, L181
 Antiochos, S. K., DeVore, C. R., & Klimchuk, J. A. 1999, *ApJ*, 510, 485
 Antiochos, S. K., Karpen, J. T., & DeVore, C. R. 2002, *ApJ*, 575, 578
 Aulanier, G., DeLuca, E. E., Antiochos, S. K., McMullen, R. A., & Golub, L. 2000, *ApJ*, 540, 1126
 Berger, M. A. 1984, *Geophys. Astrophys. Fluid Dyn.*, 30, 79
 Berger, M. A., & Field, G. B. 1984, *J. Fluid Mech.*, 147, 133
 Bieber, J. W., & Rust, D. M. 1995, *ApJ*, 453, 911
 Boris, J. P. 1970, *NRL Memorandum Rep.* 2167
 Carmichael, H. 1964, in *The Physics of Solar Flares*, ed. W. N. Ness (NASA SP-50; Washington: NASA), 451
 Chen, J. 2001, *Space Sci. Rev.*, 95, 165
 Demoulin, P., et al. 2002, *A&A*, 382, 650
 DeVore, C. R. 1991, *J. Comput. Phys.*, 92, 142
 ———. 2000, *ApJ*, 539, 944
 Finn, J. M., & Antonsen, T. M. 1985, *Comments Plasma Phys. Controlled Fusion*, 9, 111
 Forbes, T. G. 2000, *J. Geophys. Res.*, 105, 23153
 Forbes, T. G., & Isenberg, P. A. 1991, *ApJ*, 373, 294
 Furth, H. P., Killeen, J., & Rosenbluth, M. N. 1963, *Phys. Fluids*, 6, 459
 Gallagher, P. T., Lawrence, G. R., & Dennis, B. R. 2003, *ApJ*, 588, L53
 Gopalswamy, N., Lara, A., Yashiro, S., & Howard, R. A. 2003, *ApJ*, 598, L63
 Hirayama, T. 1974, *Sol. Phys.*, 34, 323
 Karpen, J. T., Antiochos, S. K., & DeVore, C. R. 1996, *ApJ*, 460, L73
 Klimchuk, J. A. 2001, in *Space Weather*, ed. P. Song, G. Siscoe, & H. Singer (Geophys. Monogr. 125; Washington: AGU), 143
 Kopp, R. A., & Pneuman, G. W. 1976, *Sol. Phys.*, 50, 85
 Kumar, A., & Rust, D. M. 1996, *J. Geophys. Res.*, 101, 15667
 Lin, J., Raymond, J. C., & van Ballegoijen, A. A. 2004, *ApJ*, 602, 422
 Lin, J., Soon, W., & Baliunas, S. L. 2003, *NewA Rev.*, 47, 53
 Low, B. C. 1996, *Sol. Phys.*, 167, 217
 ———. 2001, *J. Geophys. Res.*, 106, 25141
 Low, B. C., & Smith, D. F. 1993, *ApJ*, 410, 412
 Mikić, Z., & Linker, J. A. 1994, *ApJ*, 430, 898
 Moore, R. L., & Roumeliotis, G. 1992, in *Eruptive Solar Flares*, ed. Z. Svestka, B. V. Jackson, & M. E. Machado (New York: Springer), 69
 Nindos, A., Zhang, J., & Zhang, H. 2003, *ApJ*, 594, 1033
 Patty, S. R., & Hagyard, M. J. 1986, *Sol. Phys.*, 103, 111
 Priest, E. R., & Forbes, T. 2000, *Magnetic Reconnection* (Cambridge: Cambridge Univ. Press)
 Rust, D. M. 2001, *J. Geophys. Res.*, 106, 25075
 Schmieder, B., Demoulin, P., Aulanier, G., & Golub, L. 1996, *ApJ*, 467, 881
 Shibata, K., Nowaza, S., & Matsumoto, R. 1992, *PASJ*, 44, 265
 Sterling, A. C., & Moore, R. L. 2001, *ApJ*, 560, 1045
 Sturrock, P. A. 1966, *Nature*, 211, 695
 ———. 1989, *Sol. Phys.*, 121, 387
 ———. 1991, *ApJ*, 380, 655
 Taylor, J. B. 1974, *Phys. Rev. Lett.*, 33, 1139
 van Ballegoijen, A., & Martens, P. C. H. 1989, *ApJ*, 343, 971
 Wang, H., Ewell, M. W., Jr., Zirin, H., & Ai, G. 1994, *ApJ*, 424, 436
 Wolfson, R., & Saran, S. 1998, *ApJ*, 499, 496
 Woltjer, L. 1958, *Proc. Natl. Acad. Sci.*, 44, 489
 Wu, S. T., Guo, W. P., & Wang, J. F. 1995, *Sol. Phys.*, 157, 325
 Zhang, J., Dere, K. P., Howard, R. A., Kundu, M. R., & White, S. 2001, *ApJ*, 559, 452